PROCEEDINGS A

rspa.royalsocietypublishing.org

Research

Check for updates

Article submitted to journal

Subject Areas:
Applied Mathematics

Keywords:
matrix Wiener–Hopf method, Mindlin plate, flexural waves, diffraction

Author for correspondence:
Ian Thompson
e-mail: ian.thompson@liverpool.ac.uk

Electronic Supplementary material for 'Diffraction by a rigid strip in a plate modelled by Mindlin theory'

Ian Thompson

Department of Mathematical Sciences,
University of Liverpool, Liverpool L69 7ZL, UK

THE ROYAL SOCIETY
PUBLISHING

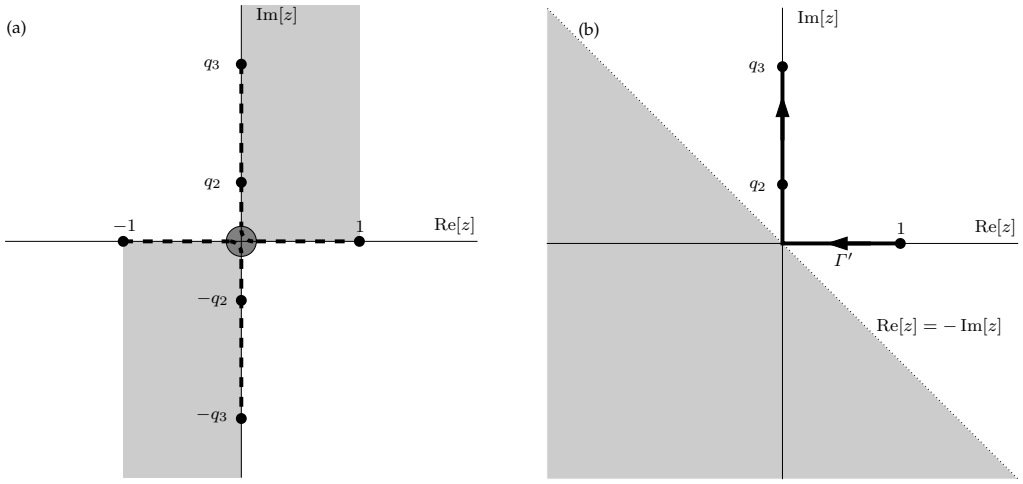

Figure S1. (a) Adjusted branch cuts chosen such that scalar kernel is zero free. The lightly shaded regions show where the change in cut configuration from figure 2a in the main body of the paper affects the value of K. The radius of the dark circle (ϵ) is such that $K(z) \neq 0$ for $|z| < \epsilon$. (b) The contour Γ' used in computing the scalar kernel factors. The variable α lies in the shaded region.

S1. Factorisation of the scalar kernel

To transform the kernel factorisation integral (6.2) into a form useful for numerical computation, it is necessary to deform the paths of integration. Zeros of $K(z)$ could interfere with this process, but we can rule these out as follows. First, from (5.14), we observe that $K(0) = -|q_3|(A_2|q_2| + \mathrm{i}A_1)$, which is clearly nonzero. Hence there exists $\epsilon > 0$ such that $K(z) \neq 0$ for $|z| < \epsilon$. Next, we reposition the branch cuts emanating from ± 1 to run along the real and imaginary axes, joining 1 to q_2 and -1 to $-q_2$. Near the origin, we use curved indentations that lie inside the circle $|z| < \epsilon$. Since the multivalued components of $K(z)$ are the products $\gamma_1\gamma_3$ and $\gamma_2\gamma_3$, neither of which has a branch point at infinity, the cuts above q_3 and below $-q_3$ now disappear, and the new configuration is as shown in figure S1a. The paths of integration ($\Gamma^{\pm}$ in (6.2)) can pass between the curved sections of the cuts, so that their orientation with respect to all of the branch points is preserved.

We may now use the principle of the argument [1, section 7.3] to prove that K is zero-free on the primary sheet of the Riemann surface. We begin by observing that (5.15) now holds as $\alpha \to \infty$ in any direction, because we are using finite branch cuts. Consequently, $\log[K(z)]$ will return to its original value if z traverses a circle of radius N, centred at the origin, provided N is sufficiently large. To complete the proof, it is sufficient to show that $K(z)$ cannot be real and negative on the faces of the branch cuts. It then follows $\log[K(z)]$ remains unchanged after z encircles the branch cuts, because there can be no winding around the origin in the K plane. For $z = v$ and $z = \mathrm{i}q_2 v$ with $-1 < v < 1$, γ_1 is strictly negative imaginary whereas all other terms in K are real. Therefore $K(z)$ cannot be real here. The remaining sections of the cuts can be handled in a similar way, making use of the inequalities (2.15).

Next, we observe that K is an even function, so it follows from (6.2) that $K^+(\alpha) = K^-(-\alpha)$. Since we also have the relationship $K(\alpha) = K^+(\alpha)K^-(\alpha)$, it is sufficient to determine $K^-(\alpha)$ in the region $\mathrm{Re}[\alpha] < -\mathrm{Im}[\alpha]$. To achieve this, we deform the contour Γ^+ upwards. Letting $\epsilon \to 0$ leaves an integral along the faces of the 'L' shaped cut in the upper half-plane, which we denote by Γ'. This consists of straight lines from $z = 1$ to the origin and then to $z = q_3$ (see figure S1b). Then (6.2) becomes

$$K^-(\alpha) = \sqrt{K_\infty}\,\exp\left[\frac{1}{2\pi\mathrm{i}}\int_{\Gamma'}\left\{\log\left(\frac{K_\ell(z)}{K_\infty}\right) - \log\left(\frac{K_r(z)}{K_\infty}\right)\right\}\frac{\mathrm{d}z}{z-\alpha}\right], \tag{S1}$$

where the subscripts 'ℓ' and 'r' refer to evaluation on the left and right faces of the cut, respectively. Note that Γ^+ in (6.2) is traversed from left to right, and passes below the 'L' shaped cut, whereas Γ' is traversed from right to left, so that a factor -1 is introduced to the term involving K_ℓ. Since $K(z)/K_\infty$ cannot be negative real on the faces of the cuts, we may take principal values for both logarithms. On the left face of the cut, values of the functions γ_j are unchanged from the original configuration in figure 2a in the main body of the paper. Therefore $\gamma_1\gamma_3$ is negative imaginary, whereas $\gamma_2\gamma_3$ may be positive real or negative imaginary. On the right face of the cut, the real terms are the same as those on the left face but the imaginary terms switch sign, so that $K_r(z) = \overline{K}_\ell(z)$. Therefore,

$$K^-(\alpha) = \sqrt{K_\infty}\,\exp\left[\frac{1}{\pi}\int_{\Gamma'} \arg[K_\ell(z)]\frac{\mathrm{d}z}{z-\alpha}\right], \tag{S2}$$

where the argument is a principal value.

Finally, we address the fact that α may lie close to the integration contour. Since there are no branch points at $\pm q_3$ in the Kirchhoff problem (see §8), we also cause the contribution from the path joining q_2 to q_3 to disappear as $\omega \to 0$. We begin by splitting Γ' into two parts: Γ_1' joining $z = 1$ to the origin and then to q_2, and Γ_2' joining q_2 to q_3. Now (S2) is only used for values of α on or to the left of the line $\mathrm{Re}[\alpha] = -\mathrm{Im}[\alpha]$. Therefore, for the purpose of numerical integration, α may lie close to Γ_1' but not to Γ_2'. Also, since $A_j \to -1$ as $\omega \to 0$, it follows from (5.14) that $K_\ell(z)$, the value of the scalar kernel on the left face of the branch cut, is positive imaginary for $z \in \Gamma_2'$ in the low frequency limit. In view of this, we write

$$\int_{\Gamma'} \arg[K_\ell(z)]\frac{\mathrm{d}z}{z-\alpha} = \int_{\Gamma_1'}\Big(\arg[K_\ell(z)] - \arg[K(\alpha)]\Big)\frac{\mathrm{d}z}{z-\alpha} + \int_{\Gamma_2'}\Big(\arg[K_\ell(z)] - \frac{\pi}{2}\Big)\frac{\mathrm{d}z}{z-\alpha} + H(\alpha), \tag{S3}$$

where

$$H(\alpha) = \arg[K(\alpha)]\int_{\Gamma_1'}\frac{\mathrm{d}z}{z-\alpha} + \frac{\pi}{2}\int_{\Gamma_2'}\frac{\mathrm{d}z}{z-\alpha} \tag{S4}$$

$$= \arg[K(\alpha)]\log\left(\frac{\alpha-q_2}{\alpha-1}\right) + \frac{\pi}{2}\log\left(\frac{\alpha-q_3}{\alpha-q_2}\right). \tag{S5}$$

Since the variation in the argument of $z-\alpha$ cannot exceed π as z traverses either contour in (S4), both logarithms in the last expression are principal values. The remaining integrals in (S3) are suitable for numerical evaluation. The implementation used to produce the numerical results in the main body of the paper employs mappings as in (A11)–(A13) to remove end-point square root singularities, and applies the seven point Gaussian quadrature rule with adaptive refinement. In this way, the kernel factors are computed to near machine precision. The second integral vanishes from the right-hand side of (S3) in the limit $\omega \to 0$, and the last term produces a multiplicative factor $(\alpha-q_3)^{1/2}(\alpha-q_2)^{-1/2}$ in $K^-(\alpha)$ so that the branch points at $\pm q_3$ disappear from the Wiener–Hopf equation in this limit.

S2. Implementation of the implicit quadrature method

The main obstacle to numerically evaluating the solution to the matrix problem discussed in §7 of the main paper relates to the location of nodes for use in the implicit quadrature scheme. Choosing the nodes a priori leads to a simple implementation but does not control errors in an efficient way. Instead, we use an adaptive scheme that works as follows. First, the integration contours are each divided into four sections, using the vertices

$$\pm 1, \quad \pm(1+q_2)/2, \quad \pm q_2, \quad \pm(q_2+q_3)/2 \quad \text{and} \quad \pm q_3. \tag{S1}$$

The end-point singularities are removed using (A11)–(A13). A small set of nodes is then generated by applying a single step of a quadrature rule to each integral in the s plane. A second set of nodes

is generated by applying the same quadrature rule in two equal steps. The resulting linear systems are solved, and contributions to $\tilde{S}_j^+(\alpha)$, $\tilde{w}^-(\alpha)$ and $\tilde{\psi}_x^-(\alpha)$ from each section are calculated for a set of test points. Errors in the initial estimates can be computed using the second set of nodes, since these produce more accurate results. Nodes on subintervals for which the results meet a specified tolerance are retained, and subintervals on which the errors are too large are bisected again. This process is repeated until all results satisfy the tolerance condition. Using code written in Fortran 2003, running at double precision and configured to use the seven point Gaussian rule, a linear system sufficient to provide results accurate to ten significant figures was formed and solved in under 30 seconds on a six core machine running at 3GHz. Typically the number of nodes required was around one thousand. Almost all of the CPU time was used in solving the necessary linear systems; the CPU time used by other components of the implementation is very small in comparison.

Having applied the implicit quadrature method, the functions $\tilde{S}_j^+(\alpha)$, $\tilde{w}^-(\alpha)$ and $\tilde{\psi}_x^-(\alpha)$ can be evaluated using their Cauchy integral representations. A useful test at this stage is to compute both sides of the Wiener–Hopf equation (7.13) and compare their values. We can also make use of (7.13) to avoid the situation in which quadrature becomes inaccurate due to branch cut proximity. The strategy is similar to the use of the identity $K^+(\alpha) = K^-(-\alpha)$ in the scalar problem, above. We begin by dividing the plane across the line $\mathcal{L} : \operatorname{Im}\alpha = -|q_2| \operatorname{Re}\alpha$. On and to the right of $\mathcal{L}$, we compute $\tilde{S}_j^+(\alpha)$ directly by quadrature. To the left of the line $\mathcal{L}$, we compute $\tilde{w}^-(\alpha)$ and $\tilde{\psi}_x^-(\alpha)$ by quadrature. It follows from (7.16) that the removable singularity disappears from (7.13) upon multiplication by M^{-1}. Therefore we may compute $\tilde{S}_j^+(\alpha)$ from $\tilde{w}^-(\alpha)$ and $\tilde{\psi}_x^-(\alpha)$, including near the origin. If $\alpha \approx \alpha_0$ then (viewed as an equation for determining $\tilde{S}_j^+(\alpha)$), (7.13) is subject to cancellation. In most cases this issue can be avoided by simply computing $\tilde{S}_j^+(\alpha)$ directly by quadrature. Both methods for computing $\tilde{S}_j^+(\alpha)$ may be inaccurate if $\alpha_0 \approx -1$ and $\alpha \approx \alpha_0$ simultaneously. In practice this is unimportant because the cancellation in (7.13) leads to a magnification of error roughly proportional to $(\alpha - \alpha_0)^{-1}$, which does not cause all precision to be lost. However, the issue can be avoided entirely by using (7.11) and (5.21) in (5.18) to obtain

$$S_1^+(\alpha) = \frac{-\gamma_1^+(\alpha)}{(\alpha-\alpha_0)K(\alpha)}\left[A_2\big(\gamma_2(\alpha)\gamma_3(\alpha) - \alpha^2\big)\tilde{w}^-(\alpha) + \frac{\mathrm{i}\alpha\gamma_1^-(\alpha)\tilde{\psi}_x^-(\alpha)}{\gamma_2^-(\alpha)}\right], \tag{S2}$$

after which the diffraction coefficient can be evaluated using (9.6).

S3. Steepest descents analysis

To apply the method of steepest descents to the diffraction integral (4.13), it is necessary to consider the effects that singularities may have on the process of deforming the integration contour. Writing

$$\gamma_j(\alpha)|\sin\theta| + \mathrm{i}\alpha\cos\theta = -\mathrm{i}q_j + v, \quad v \geq 0, \tag{S1}$$

we find that the descent paths can be parametrised via

$$\alpha = -\cos\theta(q_j + \mathrm{i}v) \pm \sin\theta(v^2 - 2\mathrm{i}q_j v)^{1/2}, \quad v \geq 0. \tag{S2}$$

First consider the case $j = 1$, shown in figure S2a. If $x < 0$ so that $\cos\theta < 0$, the steepest descents path lies predominantly in the upper half-plane, and there are no branch points to obstruct the deformation process (as $\sin\theta \to 0$ the path wraps tightly around the cut emanating from $\alpha = q_1 = 1$). The pole at $\alpha = \alpha_0$ may lie to the right of the saddle point if $\cos\Theta < 0$, in which case its residue must be collected, but this is addressed in the main body of the article. If $x > 0$, then a diversion is required if the descent path crosses the imaginary axis at or below $-q_2$, in order to retain the correct orientation with respect to the branch point. Writing $\alpha = -\mathrm{i}u$ with $u > 0$ in (S2) shows that this occurs if $|\cot\theta| > |q_2|$. The largest contribution comes from the branch point itself, and here

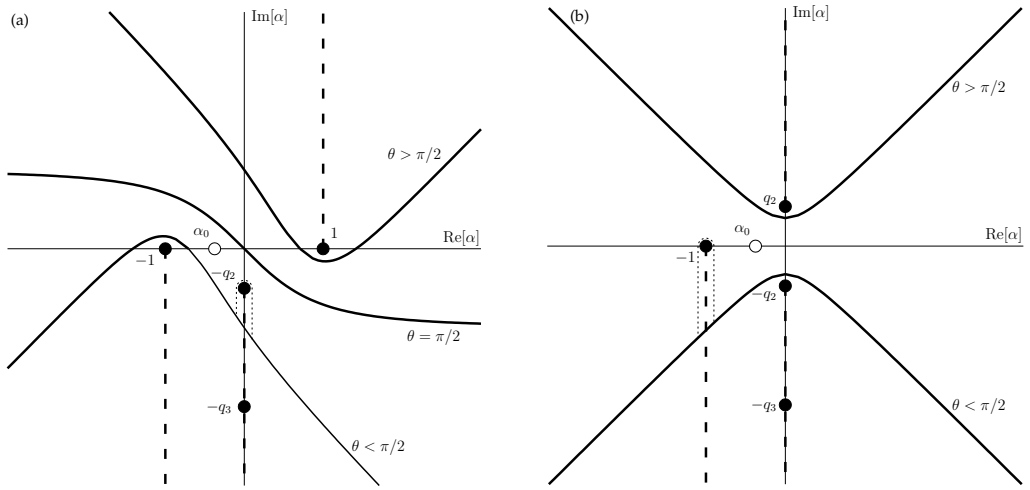

Figure S2. Steepest descents paths for (a) w_1 (b) w_2. The dotted lines show the diversions around branch points needed for certain observation angles θ. Note that the descent path for w_2 in the case $\theta = \pi/2$ is simply the real line.

the real part of the exponent is

$$r|q_2|\cos\theta > \frac{r\,|q_2|^2}{\sqrt{1+|q_2|^2}}. \tag{S3}$$

Consequently, this contribution is exponentially small unless $q_2 \approx 0$, which occurs at high frequencies, such that the Mindlin model itself breaks down (see §2). Therefore we may disregard the contribution from this diversion; the most significant contributions to w_1 are due to the pole and the saddle.

The case $j = 2$ in (S2), shown in figure S2b, is similar though slightly more complicated. Since q_2 is positive imaginary, (9.4) shows that the integrand is exponentially small at the saddle point. For $x < 0$, the steepest descents path lies in the upper half-plane. Since the only singularity in the upper half-plane is the branch point at $\alpha = q_2$, there are no obstructions to deforming the integration contour onto the steepest descents path, and we may conclude that $w_2 = O(\mathrm{e}^{-|q_2|r})$. For $x > 0$, the steepest descents path lies in the lower half-plane, and the residue from $\alpha = \alpha_0$ is collected. The branch point at $\alpha = -q_3$ does not interfere with the deformation of the path, but there is also a branch point at $\alpha = -1$, and the steepest descents path must be diverted around this. Now

$$\gamma_2(-1)|\sin\theta| - \mathrm{i}\cos\theta = \sqrt{1-q_2^2}\,|\sin\theta| - \mathrm{i}\cos\theta, \tag{S4}$$

meaning this contribution is exponentially small unless $\sin\theta \approx 0$. For θ close to zero or 2π, the branch point contribution is typically $O(r^{-3/2})$, because it can be related to an integral of the form $\int_0^\infty \sqrt{s}\mathrm{e}^{-rs}\,\mathrm{d}s$. This changes if the pole at $\alpha = \alpha_0$ lies close to the branch point, in which case the contribution is $O(r^{-1/2})$, meaning the diversion does contribute to the field at leading order. This pole is only present for $y < 0$ (see §9). Thus w_2 can contribute to the diffracted field at leading order if $\Theta \approx 0$ and $\theta \approx 2\pi$. This is related to the breakdown of the uniform approximation (9.9) near the boundary in cases where $\Theta \approx 0$, noted in §9.

References

1. Wunsch AD. 2004 *Complex Variables with Applications*. Addison–Wesley third edition.